Project Title:

Crystal Structure Prediction and High-temperature Superconductivity of Li-RE-H System at High Pressures

Name:

Yanming MA (1), Ryotaro ARITA (1), ○Toshiaki IITAKA (2)

Laboratory at RIKEN:

(1) RIKEN Center for Emergent Matter Science, First-Principles Materials Science Research Team,
(2) RIKEN Center for Computational Science, Discrete Event Simulation Research Team

1. Background and purpose of the project, relationship of the project with other projects

The search for room-temperature superconductivity has been a long-standing scientific endeavor ever since Heike Kamerlingh Onnes discovered in 1911 that mercury could conduct electricity without resistance below a critical temperature around 4 K. Twenty-four years after the discovery of this phenomenon known as superconductivity, Wigner and Huntington proposed that molecular hydrogen could undergo a phase transition into an atomic metallic hydrogen (AMH) phase at high pressures, which attracted great interest, especially after the conjecture of its ability to host very hightemperature superconductivity. Creating AMH, however, has proven extremely challenging due to the stringent synthesis and characterization conditions at very high pressures, currently recognized to be above 500 GPa. An early study found that hydrogen-rich metal hydride Th_4H_{15} was superconducting with a critical temperature T_c of 8 K at ambient pressure; later studies found that chemical substitution or doping could stabilize hydrogen-containing compounds that may host metallic and superconducting states approaching that of AMH. This line of work has been actively pursued after the conceptual development of using chemical precompression to facilitate the formation of hydrogen-dominant metallic alloys that host phonon-mediated high-temperature superconductivity.

Recent years have witnessed concerted efforts of exploring routes to achieving high-T_c superconductivity in pressure-stabilized metal hydrides (*e.g.*, refs 13−16). Following the theoretical predictions of stabilizing H_2S and H_3S at high pressures, a high T_c of 203 K at 150 GPa was documented experimentally. A different class of binary high-T_c metal (M) hydrides based on clathrate structure having stoichiometry MH_6 was predicted, led by the theoretical prediction on CaH_6. Further efforts to reach higher T_c led to the prediction and discovery of superhydrides with stoichiometries MH_n with $n > 6$. These efforts culminated in the experimental realization of superconducting LaH_{10} with a T_c of 250−260 K at pressures of 170−190 GPa, followed by YH_9 with a T_c of 243 K at 201 GPa and YH_6 with a T_c of 220 K at 166 or 237 GPa. Very recently, the long-missing clathrate structured CaH_6 predicted in 2012 was successfully synthesized in the laboratory with a measured T_c of 215 K at 170 GPa. Other notable cases of clathrate structured high-T_c hydrides include YH_{10}, Li_2MgH_{16}, and $CaYH_{12}$ from theory, and ThH_9 and ThH_{10} from experiment.

An overriding idea underlying all of these efforts is to raise the hydrogen content while at the same time ensuring that the combination of compression chemical interactions are favorable to promote the H_2 molecules in the dense structure to create material configurations closely resembling AMH in bonding environments. In this regard, a major task has thus been to find superhydrides with proper electron-rich heavy atoms that are capable of stabilizing hydrogen in a nonmolecular form to generate T_c exceeding that of the established superhydrides such as LaH_{10}.

Recent studies showed that rare-earth (RE) and actinide (An) elements are capable of maintaining

significant hydrogen by forming high-pressure clathrate compounds with a very high T_c. These results raise the exciting prospects of finding RE/An superhydrides containing even higher hydrogen content and hence further increased T_c that may approach or even exceed room temperature. Based on these considerations, we have explored electron-rich rare-earth and actinide elements that provide electrons to dissociate molecular hydrogen, thereby creating an AMH-like environment conducive to harboring high-T_c superconductivity. Using our developed structural search algorithms, we uncovered a new class of hydrogen-superrich compounds with stoichiom-etry MH_{18} (M = RE or An atom). These extreme superhydrides exhibit unique H_{36} clathrate atomic cages with bonding environments similar to that predicted for AMH. First-principles calculations for different MH_{18} superhydrides predict diverse T_c values among the same stoichiometry that offer insights into the effect and nature of chemical precompression. Notable among these extreme superhydrides are CeH_{18} and ThH_{18} that exhibit above-room-temperature T_c near 330 K at 350 GPa and 321 K at 600 GPa, respectively, which represent the highest T_c values among all hitherto known thermodynamically stable superhydrides. The results of this study provide a wealth of information on material behaviors and key physics and chemistry insights that allow an in-depth study of the factors with major influence on achieving ultrahigh-temperature phonon-mediated superconductivity in hydrides, thereby opening a path for creating binary and multinary high-T_c superhydrides that can operate at or even above room temperature.

Besides, a recent work claimed possible room-temperature superconductivity in the C−S−H system, but the structure and stoichiometry of the synthesized material remain unclear and require further investigation. we performed crystal structure searching of the C−S−H system at 300 GPa via our in-house developed CALYPSO prediction methodology. A series of metastable crystals were identified with T_c values _156 K. The coordination number of the C and S atoms in compressed C−S−H crystals are four and six, respectively, with the formation of CH_4 and SH_6 molecules, and the remaining H atoms form H_2 molecules in pairs. The formation of molecular crystals is the fundamental reason for such poor superconductivity. Besides, we searched for ground-state structures of C-doped $Im3m$–H_3S using the first-principles cluster expansion method. Superconductivity of $C_xS_{1-x}H_3$ (x = 0.0625, 0.083, and 0.10) was estimated using primitive cells containing 40–64 atoms. The doping was found to lower the density of states at the Fermi level and then decrease the T_c values accordingly. Our results provide a comprehensive map between the crystal structure and superconductivity of carbonaceous sulfur hydride materials at high pressures, which might offer a valuable reference for further exploring the superconducting mechanism.

2. Specific usage status of the system and calculation method

During the fiscal year 2022, 3.6 million CPU hours were used to investigated hydrides with high superconductivity in all these two project. We employ our developed swarm-intelligence-based CALYPSO structure prediction method, which is designed to search for the stable structures of given compounds, for the investigation of phase stability of C-S-H compounds at 300 GPa and RE-H compounds at 400 GPa. For most cases, the structure search for each chemical composition converges (evidenced by a lack of any additional structure with lower energy) after 1000~1200 structures were investigated. The energetic stability of different ternary stoichiometries is evaluated by their formation enthalpy of dissociated into the most competing element and binary compounds. The underlying energetic calculations are performed with the plane-

wave pseudopotential method as implemented in the VASP code. The Perdew-Burke-Ernzerhof generalized gradient approximation is chosen for the exchange-correlation functional. The phonon spectrum and electron-phonon coupling (EPC) of the stable compounds are calculated within the framework of linear response theory through the Quantum-ESPRESSO code, where ultrasoft pseudopotentials were used with a kinetic energy cutoff for wavefunctions of 80 Ry and a kinetic energy cutoff for charge density and potential of 1000 Ry. Electron-phonon couplings (EPC) constant λ, ω_{log}, and T_c are solved using the elk code, as derived by the direct solution of the isotropic Migdal-Eliashberg equation.

3. Result

3.1 Room-temperature superconductivity in compressed RE-H compounds

We performed structure searches in binary hydrides MH_m (m = 2–24) over a wide range of hydrogen contents to predict stable structures, with a sharp focus on hydrogen-superrich phases. Particularly noteworthy was the finding of new stoichiometric Ce and Th extreme superhydrides Ce/ThH$_{18}$ stable at experimentally accessible pressures around 300 GPa after the zero-point energy (ZPE) was considered. Specifically, CeH$_{18}$ and ThH$_{18}$ become stable at reduced pressures of 315 and 281 GPa, respectively (see Figure 1a,b), making the experimental synthesis and characterization feasible. It is noted that these newly predicted extreme superhydrides possess higher T_c with competing synthesis pressure compared to the previously proposed high-T_c binary superhydride YH$_{10}$, which was not successfully synthesized in a recent experiment. A recent work reported that materials synthesis could be achieved near terapascal pressures, making it feasible to realize the materials predicted in this work. Further calculations for a broad range of RE and An hydride compounds up to 700 GPa reveal ubiquitous stability

of the MH$_{18}$ stoichiometry among diverse RE and An hydrides for RE/An = Y, La, Ce, Ac, and Th (Figure 1b). Details of the computational methods for the structure search and property calculations are provided in the Supporting Information.
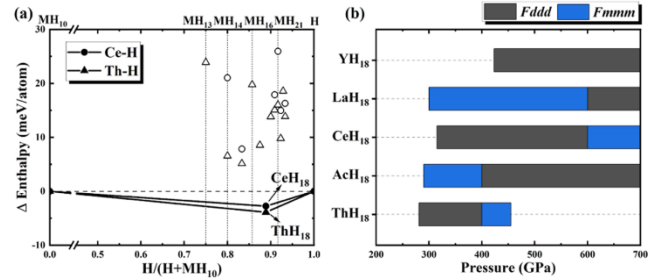

Figure 1. Calculated stability of predicted extreme superhydrides. (a) Calculated convex hull of newly identified extreme superhydrides CeH$_{18}$ and ThH$_{18}$, both in the *Fddd* structure, calculated with respect to decomposition into Ce/ThH$_{10}$ and H$_2$ at 400 GPa. Data points located on the convex hull (solid lines) represent species stable against possible decomposition. The open symbols correspond to metastable/unstable compositions identified by the search process. (b) Stable pressure ranges of the predicted extreme superhydrides MH$_{18}$ with respect to decomposition into known MH$_x$ (x = 2, 4, 6, 9, 10, 12, 16, and 17) and *Cmca*–structured H$_2$; zero-point energy (ZPE) was included in the calculations.

Conspicuous in the predicted crystal structure of the MH$_{18}$ extreme superhydrides is the H$_{36}$ clathrate cage, which contrasts with the H$_{24}$, H$_{29}$, and H$_{32}$ structural units found in previously identified hydrides with lower hydrogen contents. The peculiar three-dimensional hydrogen clathrate structure crystallizes in a unit cell with space group *Fddd* (Figure 2a) in which H$_{36}$ cages are linked by a 6H$_6$ ribbon-ring structure with two wrinkled H$_6$ hexagons above and below with bridge bonds connecting the H$_6$ hexagons to the 6H$_6$ ribbon ring (Figure 2b,c). At higher pressures, depending on the choice of the M atom, the H$_{36}$ clathrate units rearrange and stabilize in another structure with space group *Fmmm* (Figure 2b). Below we focus our analysis mainly on CeH$_{18}$ to showcase its prominent properties while also

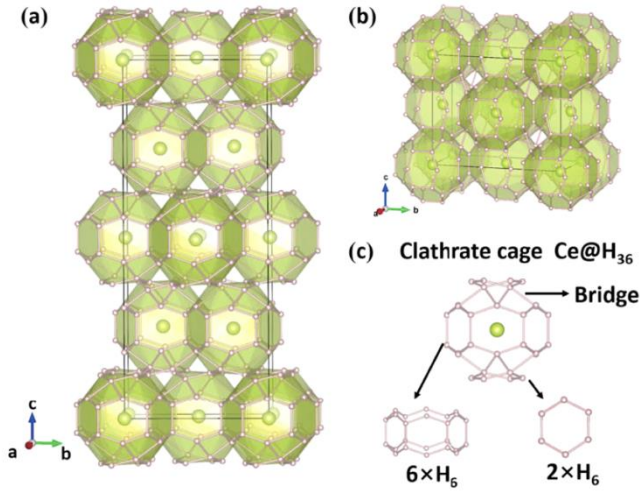discussing key data and trends involving other MH_{18} compounds.

Figure 2. Crystal structure of MH_{18}. (a) *Fddd* and (b) *Fmmm* phase. (c) Building units of the $M@H_{36}$ hydrogen clathrate cage, including a $6H_6$ ribbon ring and two H_6 hexagons, which are connected by pertinent bridge bonding networks. The large and small spheres represent the metal and hydrogen atoms, respectively.

We first examine the high-pressure electronic structure of CeH_{18}. The results clearly indicate the CeH_{18} phase is metallic with several bands crossing the Fermi level (Figure 3a, left), and hydrogen atoms make a substantial contribution to the electronic density of states (DOS) near the Fermi level, which is almost identical to the DOS contributed by the electrons from Ce (Figure 3a, right). The DOS is essentially flat around the Fermi energy, which is notably different from the DOS of LaH_{10}, which exhibits a van Hove singularity near the Fermi energy. The calculated band structures at different pressures reveal changes in band filling; notably, the hole-bands at the X-point, along the $Z–X$ path, and at the Y-point move down with increasing pressure, indicating a systematic pressure-driven electron transfer that suppresses T_c on further compression.
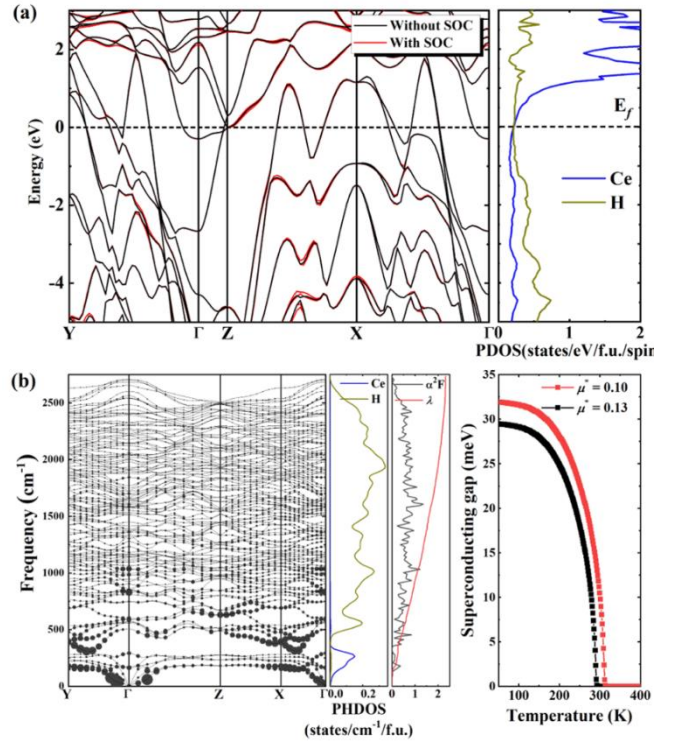

Figure 3. Electronic structures of CeH_{18}. (a) Electronic band structure (left) and projected density of states (right) of CeH_{18} at 400 GPa. The band structures without and with the inclusion of SOC are plotted with black and red lines, respectively. (b) Phonon dispersion curves with the strength of q resolved λ_q indicated by circle size (left), phonon density of states (PHDOS), Eliashberg spectral function $\alpha^2 F(\omega)$ and EPC parameter $\lambda(\omega)$ (middle), and superconducting energy gap (right) of CeH_{18} at 400 GPa.

Turning to the phonons and electron–phonon coupling in CeH_{18}, the calculated phonon dispersion results are shown in Figure 3b, left. No imaginary phonon modes are present in the entire Brillouin zone, indicating the dynamic stability of this crystal structure. We then computed the Eliashberg spectral function $\alpha^2 F(\omega)$, from which the electron–phonon coupling parameter can be obtained *via* a simple integration in the frequency domain. The resulting integrated electron–phonon coupling parameter $\lambda = 2.3$ is quite large and comparable to that found for H_3S ($\lambda = 2.2$). Such strong electron–phonon coupling makes various approximate weak-coupling T_c formulas generally unreliable, and an accurate description necessitates direct numerical solutions to

the Eliashberg equations. Adopting the latter method, we calculated superconducting energy gap and transition temperature and varied the Coulomb pseudopotential from $\mu^* = 0.10$ (as is typically used) to $\mu^* = 0.13$ to estimate a reasonable range of T_c values. The resulting T_c of 309−329 K (for $\mu^* = 0.10$ and 0.13) at 350 GPa, where CeH_{18} is stable, is well above the room temperature. These results are significantly higher than the highest T_c predicted for previously reported Ce superhydrides with lower hydrogen contents (*e.g.*, $T_c = 117$ K for CeH_9) and represent the highest predicted T_c among all known thermodynamically stable superhydrides.
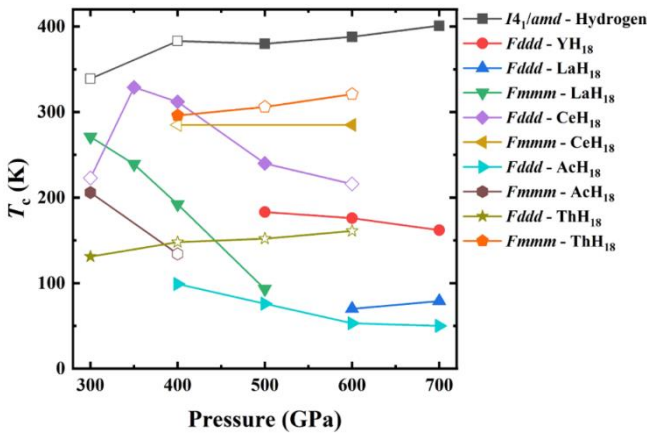

Figure 4. Superconducting critical temperatures of the predicted extreme superhydrides. Calculated T_c ($\mu^* = 0.10$) for selected extreme superhydrides MH_{18} compared with the results for the $I4_1/amd$ phase of solid hydrogen at high pressures. Solid (open) symbols represent the T_c data for stable (metastable) structural phases of the indicated MH_{18} compounds and atomic metallic hydrogen.

To elucidate the underlying mechanisms for the predicted superconductivity of these extreme superhydrides, we calculated electronic, phonon, and electron−phonon coupling parameters, and the resulting critical temperatures using the Eliashberg equations of other selected MH_{18} compounds. We also performed identical calculations for pure AMH in the $I4_1/amd$ structure, which is predicted to be stable or metastable in the same pressure range. First, we note that systematic examination of the energetics and dynamic stability of the MH_{18} structures beyond their

stability fields reveal meta-stability to lower pressures of phases that maintain high superconducting temperatures (Figure 1b). The pressure dependence of T_c for the identified stable and metastable phases of MH_{18} and $I4_1/amd$ hydrogen is given in Figure 4. The T_c values are distributed over a large range, from 50 K for $Fddd$-AcH_{18} at 700 GPa up to near 330 K for $Fddd$-CeH_{18} at 350 GPa ($\mu^* = 0.10$). Moreover, the resulting critical temperatures vary considerably among the MH_{18} superhydrides at the same pressure. The associated microscopic properties of each phase listed in Table 1 detail the differences in superconducting behavior among the compounds. The disparities within the same stoichiometry and clathrate structures stem from their characteristic vibrational frequencies, electron−phonon coupling parameters λ, and electronic DOS at the Fermi level $N(E_f)$. We also have calculated the charge transfer for CeH_{18} and LaH_{18}, and the results show charge transfer from metal Ce/La to hydrogen atoms. The T_c values for different MH_{18} structures may also be related to the different f electron fillings, *e.g.*, there are different T_c values for different MH_{10} superhydrides as previously reported.

The present findings offer important clues for understanding the trends in superhydride T_c values that approach that of AMH at high pressures. Among the extreme superhydrides, CeH_{18} exhibits the highest T_c over the entire pressure range, with nearest-neighbor H−H distances of 0.85−1.17 Å, close to that of $I4_1/amd$ structured AMH (1.0 Å) at 500 GPa. The calculated projected phonon DOS from the Ce and H atoms (Figure 3b) shows that the main contributions to the EPC come from the mid- and high-frequency hydrogen vibrations at 500−2500 cm^{-1}. Further, most of MH_{18} compounds exhibit monotonically decreasing T_c with increasing pressure, the exception being both $Fddd$- and $Fmmm$-ThH_{18} for which T_c slightly increases on compression. The decrease in T_c with pressure of most superhydrides is reminiscent of the behavior of AMH at higher

pressures (700−1,000 GPa), which is consistent with the idea that chemical precompression in hydrogen compounds shifts their material behavior toward lower pressures. These insights are helpful for continued exploration and rational design of optimal superconducting superhydrides.

Table 1. Superconductivity of Predicted Structures[a]

compound	P	λ	$\omega_{\log}$	$N(E_f)$	T_c	$T_c(SOC)$
H-$I4_1/amd$	300	2.34	1577	0.23	339(320)	
H-$I4_1/amd$	400	2.39	1719	0.25	383(362)	
H-$I4_1/amd$	500	2.24	1806	0.23	380(356)	
H-$I4_1/amd$	600	2.10	1953	0.23	388(362)	
H-$I4_1/amd$	700	2.08	2021	0.25	401(375)	
YH$_{18}$-$Fddd$	500	1.50	1082	0.22	183(165)	
YH$_{18}$-$Fddd$	600	1.28	1467	0.21	176(158)	
YH$_{18}$-$Fddd$	700	1.10	1704	0.20	162(140)	
LaH$_{18}$-$Fddd$	600	0.74	1638	0.16	70(55)	
LaH$_{18}$-$Fddd$	700	0.78	1642	0.17	79(64)	
LaH$_{18}$-$Fmmm$	300	2.46	1156	0.25	271(255)	
LaH$_{18}$-$Fmmm$	350	1.68	1491	0.23	239(222)	
LaH$_{18}$-$Fmmm$	400	1.28	1649	0.22	192(174)	
LaH$_{18}$-$Fmmm$	500	0.82	1663	0.17	93(76)	
CeH$_{18}$-$Fddd$	300	2.03	985	0.27	223(207)	224(208)
CeH$_{18}$-$Fddd$	350	2.80	919	0.32	329(309)	330(310)
CeH$_{18}$-$Fddd$	400	2.32	1294	0.33	312(292)	310(290)
CeH$_{18}$-$Fddd$	500	1.85	920	0.27	240(212)	
CeH$_{18}$-$Fddd$	600	1.64	844	0.26	216(194)	
CeH$_{18}$-$Fmmm$	400	2.21	1260	0.22	285(265)	
CeH$_{18}$-$Fmmm$	600	1.76	1388	0.22	285(262)	
AcH$_{18}$-$Fddd$	400	0.92	1411	0.18	99(83)	
AcH$_{18}$-$Fddd$	500	0.80	1480	0.17	76(62)	
AcH$_{18}$-$Fddd$	600	0.65	1718	0.17	53(40)	
AcH$_{18}$-$Fddd$	700	0.62	1844	0.18	50(37)	
AcH$_{18}$-$Fmmm$	300	1.68	1217	0.23	206(190)	
AcH$_{18}$-$Fmmm$	400	1.36	904	0.20	134(119)	
ThH$_{18}$-$Fddd$	300	1.15	1227	0.21	131(116)	
ThH$_{18}$-$Fmmm$	400	3.39	568	0.37	296(277)	296(277)
ThH$_{18}$-$Fmmm$	500	1.92	1573	0.40	306(284)	306(285)
ThH$_{18}$-$Fmmm$	600	2.13	1331	0.42	321(299)	321(299)

[a]Calculated pressure (P (GPa)) variation of λ, $\omega_{\log}$ (K), $N(E_f)$ (states/Ry/atom/spin) and T_c (K) for $\mu^* = 0.10(0.13)$ for selected MH$_{18}$ compounds in $Fmmm$ or $Fddd$ phase and hydrogen in the $I4_1/amd$ structure.

We consider additional effects such as spin−orbit coupling (SOC), magnetism, and electron correlation that may affect the estimated T_c of the predicted MH$_{18}$ compounds. We take the highest T_c extreme superhydrides CeH$_{18}$ and ThH$_{18}$ as examples to assess these effects. Our calculations reveal that the T_c values are insensitive to SOC (Table 1), which is consistent with the nearly identical band structures

calculated with and without the SOC (Figure 3a). We examined the energetics of the magnetic structures of the predicted MH$_{18}$ compounds by considering six possible magnetic configurations (one ferromagnetic and five antiferromagnetic configurations). The results show that the nonmagnetic state is the most stable among all of the predicted MH$_{18}$ compounds. A recent work quantified the correlation between the f orbital states at the Fermi energy with T_c for the lanthanide hydrides. These results offer insights into the reason for CeH$_{18}$ and ThH$_{18}$ hosting high T_c values due to the fact that both Ce and Th elements have less partially filled f electron states. Although we have not considered electron correlation effects on the EPC due to a lack of available computational tools, we note that previous studies have shown that the experimental results on several hydrides and superhydrides (e.g., those of La, Y, Th, and Ca) are well described by the theoretical results obtained within the current EPC computation scheme without considering the electron correlation effects. On this basis, it is expected that the results in the present work offer a reasonably accurate description of the superconductivity in the newly predicted MH$_{18}$ compounds. For other RE/An hydrides that are not discussed in this work, especially those with more filled f electron states, it is expected that the magnetic, SOC, and strong correlation effects play more prominent roles, and other hydrogen-rich superconducting hydrides cannot be ruled out. However, phonon-mediated superconductivity is unlikely to be the underlying mechanism in these systems, and related studies are beyond the scope of this work.

3.2 High-temperature superconductivity in C-S-H compound at 300 GPa

Based on the results from the variable-composition crystal structure searches and the cluster expansion, we constructed the ternary phase diagram of C–S–H as presented in Fig. 1(a). Unfortunately, no

thermodynamically stable C–S–H compounds were found, indicating all the ternary compounds tend to decompose into elements and binaries under certain conditions. Nevertheless, in previous high-throughput material discovery studies, the convention for the threshold between metastable (likely to be synthesized) and unstable (unlikely to be synthesized) compounds is 50 meV/atom. The same convention was adopted in this work. Therefore, metastable C–S–H compounds cannot be precluded from experimental synthesis.
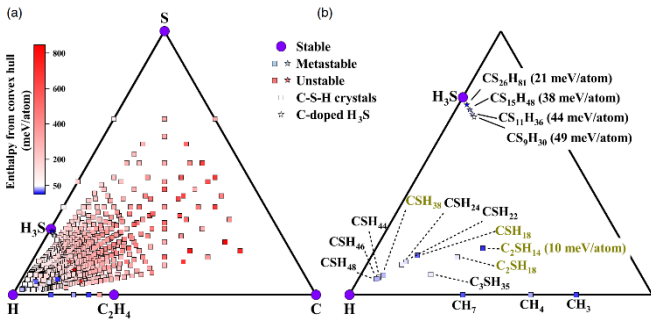

FIG. 1. (a) Calculated stabilities of $C_xS_yH_z$ relative to C, S, H, and binary compounds at 300 GPa. H-rich molecular crystals and H_3S-like structures with low levels of carbon doping are presented with squares and stars, respectively. A square (or star) filling with blue or red indicates that the corresponding ternary compound is metastable or unstable. Purple circles indicate stable phases. (b) Metastable C–S–H compounds with formation enthalpies below 50 meV/atom at 300 GPa. Labels in gold or black indicate the corresponding ternary compounds are insulated or metallic.

We found that C–S–H compounds with high-H content or a low level of carbon doping are more stable than other compositions. Specifically, there are ten H-rich ternaries and four low-level C-doping compounds that are metastable with formation enthalpies lower than 50 meV/atom at 300 GPa [as shown in Fig. 1(b), formation enthalpies and structural parameters of these metastable compounds are listed in Table S1]. Among of which $P3$–C_2SH_{14} has the lowest enthalpy of decomposition at 300 GPa [10 meV/atom above the convex hull, as shown in Fig. 1(b)]. Further pressure may help to

reduce the formation enthalpy and stabilize the new compound, calculated formation enthalpy as a function of pressure is thus shown in Fig. S1, which shows that $P3$–C_2SH_{14} is not a thermodynamically stable structure at a wide range of pressures (200–400 GPa), and has the lowest enthalpy value of thermal decomposition of 6 meV/atom at 270 GPa. Then we focus on the crystal structures and superconductivity of the H-rich compounds.

TABLE I. Space group (S.G.), formation enthalpy ($\_E$, meV/atom), band gap (gap, eV), electronic density of states at the Fermi level [$N(E_f)$, states/spin/Ry/f.u.], λ, $\omega_{\log}$ (K), and T_c (K) estimated using $\mu^* = 0.10(0.13)$ for metastable C–S–H molecular crystals at 300 GPa [(M) indicates metallic phase].

Compound	S.G.	ΔE	Gap	$N(E_f)$	λ	$\omega_{\log}$	T_c
C_2SH_{14}	$P3$	10	1.65				
CSH_{18}	Cm	18	0.21				
CSH_{46} (M)	$P1$	32		4.62	0.97	1293	93(80)
CSH_{48} (M)	$P1$	35		7.58	1.56	1071	156(142)
CSH_{38}	$P1$	36	0.27				
CSH_{22} (M)	$P1$	44		2.64	0.99	1045	78(68)
C_2SH_{18}	$P\bar{1}$	45	0.79				
C_3SH_{35} (M)	$P1$	46		6.59	2.47	558	156(143)
CSH_{24} (M)	$P1$	47		4.34	2.09	595	138(125)
CSH_{44} (M)	$P1$	50		5.51	1.50	791	113(100)

These metastable H-rich C–S–H compounds are all molecule crystals composed of CH_4, SH_6, and H_2 units. C atoms form CH_4 molecule with neighboring H atoms. The valence electron configuration of the S atom is $3s^23p^4$, which makes it not surprising that the coordination number of S is six at 300 GPa, and then results in SH_6 molecule units. Other H atoms form H_2 molecules in pairs. Such molecule crystals are usually insulators and hard to be good conductors though insulation-metal phase transition may occur under high pressure. Calculations show that C_2SH_{14}, CSH_{18}, CSH_{38}, and C_2SH_{18} exhibit nonmetallic characteristics at 300 GPa with band gaps of 1.65, 0.21, 0.27, and 0.79 eV, respectively, while the other six metastable molecular crystals are metallic with T_c $\_156$ K (as shown in Table I). We discuss the structures and superconductivity of the most stable

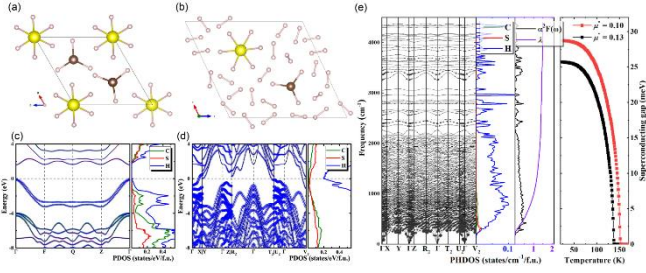C_2SH_{14} and the highest superconducting CSH_{48} as representatives of H-rich molecular crystals.

FIG. 2. Crystal structures of (a) $P3$–C_2SH_{14} and (b) $P1$–CSH_{48} at 300 GPa. The large, medium, and small spheres represent the S, C, and H atoms, respectively. CH_4, SH_6, and H_2 molecules are building units that form these two molecule crystals. Electronic band structure (left panel) and projected density of states (right panel) of (c) $P3$–C_2SH_{14} and (d) $P1$–CSH_{48} at 300 GPa. © Phonon dispersion curves with the strength of q resolved λ_q indicated by circle size, projected phonon densities of states (PHDOS), isotropic Eliashberg spectral function $\alpha^2F(\omega)$ and EPC parameter $\lambda(\omega)$, and superconducting gap of $P1$–CSH_{48} at 300 GPa.

Crystal structures of $P3$–C_2SH_{14} and $P1$–CSH_{48} are shown in Figs. 2(a) and 2(b), where the characteristics of molecular crystals are so obvious that they can be written as $(CH_4)_2(SH_6)$ and $(CH_4)(SH_6)(H_2)_{19}$, respectively. To clarify the origin of metallic properties in $P1$–CSH_{48}, electron band structures and the project electronic density of states (PDOS) of insulating $P3$–C_2SH_{14} and metallic $P1$–CSH_{48} at 300 GPa is shown in Figs. 2(c) and 2(d). Calculated results show that CH_4 and SH_6 contribute more to the deep orbitals with lower energy due to there are strong covalent bonding behavior in C–H and S–H bonds, while hydrogen atoms make a substantial contribution to the electronic density of states near the Fermi level [$N(E_f)$], indicating that the existence of a large number of H_2 units in the $P1$–CSH_{48} compound results in its metallic property. EPC calculations show an integrated electron-phonon coupling parameter λ of 1.56 at 300 GPa, which is not very large compared with the value of $\lambda = 2.2$ for H_3S.

90% of the contribution to λ is derived from the–H − H vibration modes of 250–2200 cm^{-1} [as shown in Fig. 2(e)]. T_c values of the H_2-rich hydrides, such as MgH_{16} and YH_{24}, usually not higher than that of the molecular hydrogen (T_c of $\approx$242 K at 450 GPa). Similarly, with a direct numerical solution to the Eliashberg equations, T_c of $P1$–CSH_{48} is estimated to be 142–156 K at 300 GPa, where the Coulomb pseudopotential was set to be the typical values of $\mu^\star$ = 0.10–0.13. Table shows a positive correlation between λ, $N(E_f)$, and the hydrogen content of C–S–H molecular crystals, which is consistent with the fact that the metallic and superconductivity of C–S–H molecular crystals are mainly due to the contribution of H_2 molecules. Naturally, $P1$–CSH_{48}, with the highest hydrogen content, has the highest $N(E_f)$ and thus the highest T_c value (156 K) among the six metallic molecular crys"als 'ist©d in Table I.

Next, we investigated the four metastable H_3S-like compounds with 3.7%, 6.25%, 8.3%, and 10% doped carbon, respectively, which were identified using the cluster expansion method. Primitive cells of these four H̲$_3$S-like compounds can be seen as supercells of the $Im3m$–H_3S where sulfur atoms were replaced by carbon atoms. Thus, carbon atoms here are octahedrally coordinated by six hydrogen atoms (as shown in Fig. 3). Low-level carbon-doping localizes electrons in C–H bonds and reduced symmetry, which is detrimental to high-temperature superconductivity. To investigate how different levels of carbon doping affect the stability, electronic structure, and superconductivity of C–S–H_compounds, detailed analysis were carried out on the $Pm3m$–$H_3S_{0.9375}C_{0.0625}$ ($CS_{15}H_{48}$), $C2/m$–$H_3S_{0.917}C_{0.083}$ ($CS_{11}H_{36}$), and $C2/m$–$H_3S_{0.9}C_{0.1}$ (CS_9H_{30}) stoichiometr̲ies, since the electron-phonon coupling simulations of $Im3m$– $H_3S_{0.963}C_{0.037}$ ($CS_{26}H_{81}$) exceed the limits of our current computing facilities. All of these three compounds are dynamically stable at 300 GPa and can be dynamically stable at pressures down to 260, 230, and 180 GPa, respectively (see Fig. S2 for
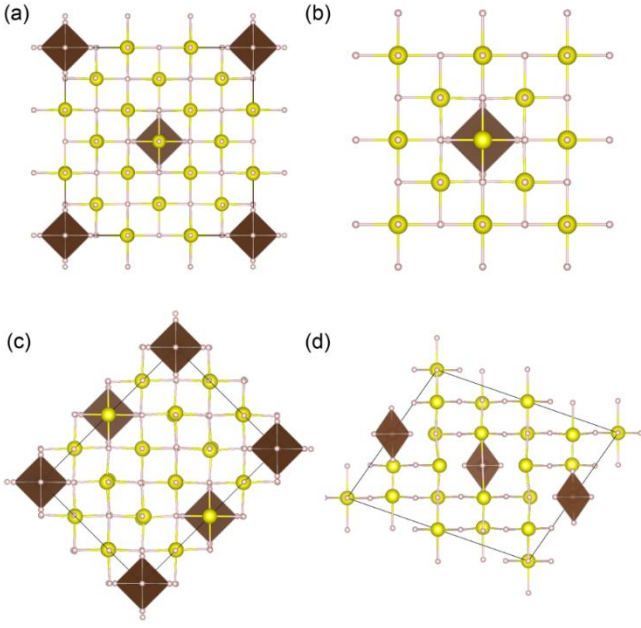
detail).

FIG. 3. Crystal structures of (a) $Im3m$–$H_3S_{0.963}C_{0.037}$ ($CS_{26}H_{81}$), (b) $Pm3m$–$H_3S_{0.9375}C_{0.0625}$ ($CS_{15}H_{48}$), (c) $C2/m$–$H_3S_{0.917}C_{0.083}$ ($CS_{11}H_{36}$), and (d) $C2/m$–$H_3S_{0.9}C_{0.1}$ (CS_9H_{30}) at 300 GPa. The large, medium, and small spheres represent the S, C, and H atoms, respectively. The translucent regular tetrahedrons represent the SH_6-like CH_6 units.

Calculated superconductivity of compressed $CS_{15}H_{48}$, $CS_{11}H_{36}$, and CS_9H_{30} is listed in Table II. To better visualize how doping affect superconductivity, $N(E_f)$, λ, and T_c (K) for C-doped H_3S compounds with different doping ratios at 300 GPa are shown in Fig. 4(a). With the increase of C-doping concentration, T_c rises first and then decreases. $CS_{11}H_{36}$ with a C-doped concentration of 8.3% has the highest T_c value. It is worth noting that, with the increase of doping concentration, T_c shows exactly the same trend as $N(E_f)$, which indicated that doping affects the $N(E_f)$ thus T_c values. Additionally, the superconducting temperature increases with decreasing pressure [as shown in Fig. 4(b)], and $CS_{11}H_{36}$ have the T_c value of 216 K at 230 GPa. Notably, the T_c values of C-doped H_3S compounds are lower than that of H_3S in the pressure range studied and are ≈100 K lower than the maximum measured value for the C–S–H superconductor, which is inconsistent with previous studies.
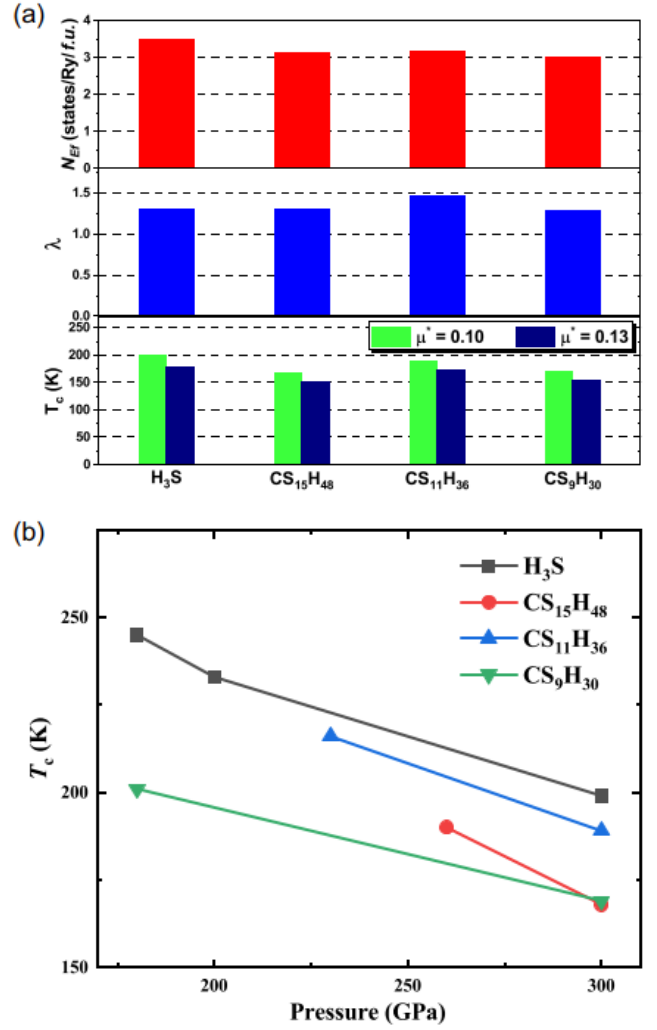

FIG. 4. (a) Calculated electronic density of states at the Fermi level [$N(E_f)$] (top panel), the electron-phonon coupling parameter (λ) (middle panel), and T_c (bottom panel) of H_3S and H_3S-like low level C-doping C–S–H compounds at 300 GPa. (b) Pressure dependence of T_c of H_3S and H_3S-like low level C-doping C–S–H compounds.

TABLE II. Primitive cells, space group (S.G.), pressure (GPa), electronic density of states at the Fermi level [$N(E_f)$], states/spin/Ry/f.u.], λ, ω_{log} (K), isotropic superconducting gap (meV) at 40 K, and T_c (K) estimated using $\mu^* = 0.10(0.13)$ for H_3S and H_3S-like low-level C-doping C–S–H compounds.

Compound	Primitive cell	S.G.	Pressure	$N(E_f)$	λ	ω_{log}	Δ	T_c
H_3S	H_3S	$Im\bar{3}m$	180	3.30	2.35	1134	51.32	245(230)
H_3S	H_3S	$Im\bar{3}m$	200	3.31	1.83	1366	45.68	233(217)
H_3S	H_3S	$Im\bar{3}m$	300	3.48	1.30	1679	35.26	199(178)
$H_3S_{0.9375}C_{0.0625}$	$CS_{15}H_{48}$	$Pm\bar{3}m$	260	3.18	1.74	900	35.07	190(168)
$H_3S_{0.9375}C_{0.0625}$	$CS_{15}H_{48}$	$Pm\bar{3}m$	300	3.14	1.30	1353	30.29	168(151)
$H_3S_{0.917}C_{0.083}$	$CS_{11}H_{36}$	$C2/m$	230	3.26	1.80	1176	41.23	216(200)
$H_3S_{0.917}C_{0.083}$	$CS_{11}H_{36}$	$C2/m$	300	3.18	1.47	1338	35.30	189(172)
$H_3S_{0.9}C_{0.1}$	CS_9H_{30}	$C2/m$	180	3.12	1.84	1104	38.79	201(187)
$H_3S_{0.9}C_{0.1}$	CS_9H_{30}	$C2/m$	300	3.01	1.29	1429	31.17	169(153)

Despite performing thorough chemical composition and crystal structure searches for the C–S–H system at 300 GPa to tackle the unsolved puzzle of room-temperature superconducting carbonaceous sulfur hydride, neither a thermodynamically stable compound nor room-temperature superconductivity was identified. We have to mention that the validity of the experimental results has recently been questioned, where it has been proposed that either the measured superconductivity in C–S–H might be unconventional or the measurements might be erroneous. Clearly, more effort is required to fully understand the measured superconductivity in carbonaceous sulfur hydride.

4. Conclusion

Extreme superhydrides represent a class of hydrogen-rich materials containing the highest atomic hydrogen content among binary metal hydrides reported to date. The structures of these MH_{18} compounds consist of unique H_{36} clathrate units stabilized under pressure starting around $300-400$ GPa. Superconducting critical temperatures exceeding room temperature arise from favorable electronic density of states near the Fermi level and the large phonon energy scale of the vibration modes, as well as the strong electron–phonon coupling, as demonstrated for CeH_{18} and ThH_{18}. Meanwhile, other MH_{18} compounds exhibit a wide range of T_c with variable combinations of electronic, phonon, and electron–phonon coupling. Recent focus in this research field has been mostly on reaching higher critical temperatures in ternary and higher multinary hydrides; the present work raises remarkable prospects that the bonding and electronic properties of the newly identified extreme binary superhydrides parallel those of

atomic metallic hydrogen, giving rise to the highest T_c values among all known thermodynamically stable superhydrides. Furthermore, we have examined the influence of various heavy elements in hydrogen-rich

superconductors over a range of pressures, and the resulting insights extend and refine the original conjecture of reducing the pressure for achieving AMH-like superconductivity by chemical doping and chemical precompression. Additional considerations of electron-[31] or hole-[47]doping effects in these extreme superhydrides may provide a promising platform for further exploration and optimization of superconductors that may host extraordinary above-room-temperature superconductivity.

In addition, we have extensively explored the phase space of carbonaceous sulfur hydrides at 300 GPa by using the CALYPSO structure prediction and cluster expansion method. Although no thermodynamically stable phase was found, several metastable crystals have been identified to be high-temperature superconductors with T_c values of 100–200 K. The coordination number of the C and S atoms in H-rich metastable C–S–H crystals are four and six, respectively, with the formation of CH_4 and SH_6 units, where the remaining H atoms form H_2 units in pairs. Such kinds of molecular crystals are apparently not good candidates for room-temperature superconductors. Using primitive cells up to 64 atoms, T_c values of H_3S-like structures with low levels of carbon doping were estimated to be _189 K for $H_3S_{0.917}C_{0.083}$ at 300 GPa, for the reason that doping localizes electrons in C–H bonds and then decreases the $N(E_f)$. Our current results provide a comprehensive map between the crystal structure and superconductivity of carbonaceous sulfur hydride materials at high pressures. More efforts, both theoretically and experimentally, are required to be done for making the mechanism of room-temperature superconducting in carbonaceous sulfur hydride clear.

5. Schedule and prospect for the future

I have been a HOKUSAI general user and wish to continue using the system. During the last fiscal year 2022, I have finished work on RE-H and C-S-H

compounds, and have published two articles on JACS and PRB, respectively. For the next fiscal year, we plan to continue using the HOKUSAI supercomputer to study the stability and superconductivity of compressed superhydrides, where new high-temperature superconductors and even room-temperature superconductors are expected to be proposed. We expect high-standard publications can be eventually achieved.

6． If no job was executed, specify the reason.

Fiscal Year 2022 List of Publications Resulting from the Use of the supercomputer

[Paper accepted by a journal]

X. Zhong, Y. Sun, T. Iitaka, M. Xu, H. Liu, R. J. Hemley, C. Chen, and Y. Ma, *Prediction of Above-Room-Temperature Superconductivity in Lanthanide/Actinide Extreme Superhydrides*, J Am Chem Soc **144**, 13394 (2022).

Y. Sun, X. Li, T. Iitaka, H. Liu, and Y. Xie, *Crystal Structures and Superconductivity of Carbonaceous Sulfur Hydrides at Pressures up to 300 GPa*, Phys Rev B **105**, 134501 (2022).

[Conference Proceedings]

[Oral presentation]

[Poster presentation]

[Others (Book, Press release, etc.)]